https://doi.org/10.5194/gchron-2021-27
Preprint. Discussion started: 20 September 2021

Calcite U-Pb dating of altered ancient oceanic crust in the North Pamir, Central Asia

Johannes Rembe1, Renjie Zhou2, Edward R. Sobel1, Jonas Kley3, Chen Jie4, Jian-xin Zhao2, Yuexing Feng2, Daryl L. Howard5

1 Institute of Geosciences, University of Potsdam, 14476 Potsdam-Golm, Germany

2 School of Earth and Environmental Sciences, The University of Queensland, St. Lucia QLD 4072, Australia

3 Department of Structural Geology and Geodynamics, Georg-August-Universität Göttingen, 37077 Göttingen, Germany

4 State Key Lab. of Earthquake Dynamics, Xinjiang Pamir Intracontinental Subduction National Field Observation and Research Station, Institute of Geology, China Earthquake Administration, X9GJ+RV Chaoyang, Beijing, China

5 The Australian Synchrotron, 800 Blackburn Rd Clayton, VIC 3168, Australia

Correspondence to: Johannes Rembe, jrembe@uni-potsdam.de

Abstract. The North Pamir, part of the western syntax of the India-Asia collision zone, preserves remnants of a poorly investigated Paleozoic intra-oceanic subduction zone. To constrain the age of this ancient ocean floor, we analyzed calcite phases in vesicular basalt and basaltic volcanic breccia with U-Pb geochronology using laser-ablation inductively-coupled-plasma mass-spectrometry (LA-ICP-MS). Calcite dating yielded Mississippian ages, mostly overlapping each other within errors. REE + Y data reveal that the basaltic host rock of the calcite and oxidizing seawater are major sources of trace elements during calcite precipitation. U-Pb ages seem to be independent of REE + Y concentrations. Our results demonstrate the potential of calcite dating to constrain the age of ancient ocean floors and provide a test of the hypothesis that a continuous early Paleozoic Kunlun Terrane extended from northern Tibet into the North Pamir.

Summary. Calcite is frequently formed during alteration processes in the basaltic, uppermost layer of juvenile oceanic crust. Weathered oceanic basalts are hard to date with conventional radiometric methods. We show in a case study from the North Pamir, Central Asia, that calcite U-Pb age data—supported by geochemistry and petrological microscopy—has the potential to date sufficiently old oceanic basalts, if the time span between basalt extrusion and latest calcite precipitation (~25 Ma) is considered.

1 Introduction

Dating the formation of ocean floor basalts provides significant constraints on the timing of various tectonic processes, given the voluminous occurrence of ocean floor basalts in ophiolites, sections of ocean plate stratigraphy and exhumed subduction complexes, and remnants of island-arcs and oceanic plateaus in ancient convergent margins. However, mafic volcanic rocks, in which zircons are sparse, are challenging to date with radiometric methods. $^{40}Ar/^{39}Ar$ dating of separated phenocrysts or groundmass is frequently attempted (e.g., Waagstein et al., 2002; Heath et al., 2018). However, ocean floor alteration (OFA) often disturbs K-Ar isotopic compositions by secondary potassium gain (Staudigel et al., 2013) or loss (Pringle, 2013), making $^{40}Ar/^{39}Ar$

https://doi.org/10.5194/gchron-2021-27
Preprint. Discussion started: 20 September 2021

dating more successful in providing high precision age data for fresh volcanic rocks but problematic if samples were affected by OFA.

Calcite veins and calcite-filled amygdules are commonly observed in submarine volcanic rocks. Studies show that calcite formation occurs during OFA by alkalinity-generating reactions, shortly after the eruption of lavas (e.g. Coogan and Gillis, 2018; Spivack and Staudigel, 1994; Coogan et al., 2016), driven by the infiltrating seawater and heat extraction from the oceanic crust. Such processes dominantly occur within ~25 Ma after rock consolidation (Coogan and Gillis, 2018). Therefore, dating the calcite phases in ocean floor volcanic rocks has the potential to constrain the timing of rock formation.

Calcite ICP-MS U-Pb dating has been applied to a range of geological problems such as dating of deformation (e.g., Nuriel et al., 2019), diagenesis, and sedimentation (e.g., Godeau et al., 2018), especially since several international reference materials were established (Roberts et al., 2017; Rasbury et al., 2021). We present the first study on calcite LA-ICP-MS U-Pb dating of Paleozoic oceanic crust. Several forms of calcite were dated from a volcanic sequence in the Carboniferous North Pamir arc (Bazhenov and Burtman, 1982). Calcite U-Pb ages are consistent with regional geological data and existing radiometric ages. With additional petrographic and geochemical data, our work sheds light on the potential of calcite U-Pb dating on ancient ocean floor volcanics and allows us to place better constraints on tectonic models of the Pamir.

2 Geological background and motivation

The North Pamir magmatic arc formed during the subduction of the Paleo-Tethys (e.g., Bazhenov and Burtman, 1982). It has been correlated with the South Kunlun Terrane in the north Tibetan West Kunlun by connecting ophiolitic sequences along the proposed Oytag–Kudi suture (e.g., Mattern et al., 1996). However, existing age dating reveals dissimilarities of key rock units in this suture in the West Kunlun compared to the North Pamir. The West Kunlun Kudi suture closed in the Silurian, as interpreted from zircon and monazite LA-ICP-MS U-Pb dating of amphibolite-facies rock (Zhang et al., 2018a).

The North Pamir arc consists of poorly dated mafic and intermediate volcanics, associated volcaniclastic rocks, and subordinate cherts. A series of leucogranites and granodiorites intruded into the arc between 360 and 314 Ma (Rembe et al., 2021). The green color of the volcanic rocks implies thorough spilitization, making them unsuitable for $^{40}Ar/^{39}Ar$ dating. An internal stratigraphy of the volcanic sequence is missing. We propose that abundant calcite associated with splitic basalts are a product of OFA. Calcite ages can serve as a constraint on the formation of ocean floor. Specifically, they provide the possibility of directly dating OFA as a proxy for the emplacement of mafic volcanic rocks.

We conducted calcite dating based on detailed petrographic and geochemical observations in order to provide age constraints on the North Pamir arc volcanic rocks and test its correlation with the West Kunlun. For that purpose, we sampled 4 specimens at 3 different localities in the Chinese Qimgan valley. Samples 17NP436a and 17NP436b are from the same locality and represent redeposited brecciated mafic volcanic rock with interstitial calcite cement that was formed during an early phase of brecciation (Figure 1a–c). Samples 15NP236 and 15NP233 are from two localities with amygdaloid-basalt, where 15NP236 was taken from a pillow basalt. We investigated amygdules filled exclusively with calcite (Figure 1e, f)

3 Methods

3.1 Petrological microscopy and X-ray fluorescence microscopy (XFM)

We carefully analyzed petrographic thin sections of all investigated samples with conventional light microscopy. We recognized well preserved primary features (see Sect. 4.1), which were then identified on the rock chips prepared for laser ablation. Detailed sample petrography raise the chances for robust, meaningful ages, as emphasized recently by Roberts et al. (2021). High resolution reflected light images indicate the position of ablation spots in Appendix A.

Additionally, we examined sample 17NP436a with scanning X-ray fluorescence microscopy (XFM). A polished slab parallel to the surface examined with LA-ICP-MS was prepared from the same rock chip. XFM maps were collected at the XFM beamline at the Australian Synchrotron (Howard et al., 2020). The incident excitation energy was 18.5 keV. Pixel size and dwell time per pixel are indicated in the figures in Appendix B.

3.2 Laser-ablation inductively-coupled-plasma mass-spectrometry (LA-ICP-MS)

Rock samples were processed at the School of Earth and Environmental Sciences, The University of Queensland. Samples were cut and mounted to round mounts with one-inch diameters. Samples mounts were polished with standard polishing procedures and finished with a 0.25 micrometer diamond suspension.

LA-ICP-MS U-Pb dating and geochemical analysis was performed at The University of Queensland following methods in Su et al. (2020) and Yang et al. (2021). We used WC01 as a secondary reference material and obtained an age of 251.8 ± 1.4 Ma (2σ), consistent with the recommended age of 254.4 ± 6.4 Ma (Roberts et al., 2017).

Laser ablation was achieved using an ASI RESOlution 193 ArF nm excimer laser system. Following evacuation of air, He carrier gas was introduced into the laser cell at a flow rate of 0.35 l/min. 0.005 l/min of N_2 gas was also introduce to the laser cell to enhance the measurement sensitivity. The gas mixture was then introduced into the plasma torch of a Thermo iCAP RQ quadruple ICP-MS with 1.06 l/min Ar nebulizer gas. No reaction gas was employed. The laser was run with a 100 µm diameter round spot at 10 Hz, with a measured instrument laser-fluence (laser pulse energy per unit area) of 2.5 J/cm^2. For U-Pb dating, each spot had 8 s of background, 20 s of data acquisition, and 15 s of wash out. For trace elemental analysis, each spot had 6 s of background, 25 s of data acquisition, and 10 s of wash out. Prior to data acquisition, ICP-MS signals were optimized during tuning. For our session, ~950 K cps of 238U counts and ~ 0.22 of 206Pb/238U were achieved for measuring NIST612 glass using line scans of 3 µm/s, 10 Hz, 50 µm round laser pit, and 3 J/cm^2.

U-Pb isotopes for geochronology (^{206}Pb, ^{207}Pb, ^{208}Pb, ^{232}Th, and ^{238}U) were measured with the following dwell times, ^{206}Pb (0.025 s), ^{207}Pb (0.055 s), ^{208}Pb (0.005), ^{232}Th (0.005 s), and ^{238}U (0.02 s). Both glass standard NIST614 and matrix-matched calcite standards were measured, bracketing unknown spots. NIST614 glass was used for correction of ^{207}Pb/^{206}Pb fractionation and instrument drift in the ^{238}U/^{206}Pb ratio (Woodhead and Hergt, 2001). Raw data were processed using Iolite software v3.64 (Paton et al., 2011). After the initial correction, a matrix-matched calcite reference material of known age was used for further correction of matrix-related mass bias impacting the measured ^{238}U/^{206}Pb ratios, following the approach described elsewhere, as summarized in

https://doi.org/10.5194/gchron-2021-27
Preprint. Discussion started: 20 September 2021

Yang et al. (2021). We used our in-house calcite reference materials (AHX-1D and AHX-1A) and one international reference material WC-1 (Roberts et al., 2017).

Trace elemental analysis was conducted in the same ablation areas as the U-Pb spots but without overlapping with U-Pb spots. ^{43}Ca was measured as an internal standard. Data reduction was conducted using the Iolite software v3.64 (Paton et al., 2011) with the Trace Element data reduction scheme. All reported concentrations were after international standardization using Ca (Ca = 40.1 %).

4 Results

4.1 Petrography and calcite occurrences

In the Chinese Qimgan valley, basaltic to andesitic volcanic rocks exhibit large amounts of calcite in amygdules, in between single lava pillows, and volcanic breccia layers (Figure 1 and Appendix A). Two samples, 15NP233 and 15NP236, are amygdaloid-basalts with published geochemistry (supplementary table S1 , Rembe et al., 2021). Samples 17NP436a and 17NP436b are from a volcanic breccia, rich in calcite cement fragments and calcite-overgrown, angular volcanic rock fragments.

Amygdules in samples 15NP233 and -236 show one generation of spary or botryoidal calcite with typical sweeping extinction under cross-polarized light (Figure 2a, b). Sample 15NP233 has vesicles up to 5 mm in diameter filled exclusively with calcite. Sample 15NP236 has much smaller vesicles, around 1 mm in diameter, filled with either calcite or zeolite. Both samples show high “Loss on Ignition” (LOI) values for whole rock geochemistry, accounting for high secondary, volatile rich mineral content (supplementary table S1). No fractures or veins cut across amygdules in these samples.

In samples 17NP436a and b, fracture pore space between basaltic rock fragments shows multiple calcite generations (Figure 2c, d). Calcite formed prior to deposition of the breccia. Specifically, isolated cement fragments are fully embedded in a fine-grained matrix (e.g., in sample 17NP436b). They may have formed in fractures of a volcanic edifice and were redeposited after its collapse. Some volcanic rock fragments show an early, hydrothermal clay layer (Figure 2c and phase 1 in Figure 2d). The fragments—or if present, the clay coating—is overgrown by a first generation of radial-fibrous calcite. Larger voids are filled with late, equant calcite. The presence of radial-fibrous and sparry, equant calcite crystals is typical of continuous calcite precipitation in a porous substratum (Gonzalez and Carpente, 1992). In a first phase, radial-fibrous calcite grows along the wall of the voids and successively reduces the porosity of the substratum, thereby hindering fluid flow. This reduces the calcite precipitation rate and the amount of nucleation, leading to larger, equant calcite crystals in the center of the voids. This model can be adopted for a first calcite phase (2 and 3 in Figure 2d). As the radial-fibrous and the equant calcite growth reflects one process, both calcite phases were chosen for ablation. Calcite filled fissures (4 in Figure 2d), associated with styloliths, were avoided. These are interpreted to reflect a later tectonic event, expressed by differential stress, pressure solution and reprecipitation of calcite in open joints. In order to better understand calcite phases, we further study 17NP436a with high-resolution synchrotron X-ray fluorescence mapping (Howard et al., 2020), following methods described in Vanghi et al. (2019). Sr maps show elevated content for the phase 2 and 3 calcite and much lower in fissure filling calcite phase 4, suggesting different geochemical regimes (Appendix B).

https://doi.org/10.5194/gchron-2021-27
Preprint. Discussion started: 20 September 2021

4.2 Calcite U-Pb geochronology and geochemistry

We obtained 839 single-spot analyses from 18 laser ablation areas (Appendix A), 3–6 ablation areas per sample (Figure 3 and Appendix C, data table in supplement table S2). Ages are calculated for individual ablation areas by linear regression in a Tera–Wasserburg plot. They overlap within the reported 2σ-error for each sample. Single-sample ages use analyses from all ablation areas (Figure 4). Volcanic breccia samples 17NP436a (Figure 4a) and 17NP436b (Figure 4b) have ages of 323.1 ± 2.0 Ma and 327.1 ± 2.8 Ma (2σ), respectively. Vesicle calcite samples 15NP233 (Figure 4c) and 15NP236 (Figure 4d) yielded ages of 330.5 ± 3.2 Ma and 353.2 ± 9.7 Ma (2σ), respectively.

For each laser ablation area, we also measured REE + Y geochemical data (a total of 380 single spot analyses) using LA-ICP-MS (data table in supplement table S3). Calcite REE patterns normalized to chondrite (Boynton, 1984) are mostly flat to slightly "U" shaped (Appendix D). REE content of the vesicle-hosted calcite is higher (61 ppm mean total REE content in sample 15NP233, 59 ppm in sample 15NP236) compared to the breccia calcite cement (8 ppm in 17NP436a and 12 ppm in 17NP436b). LREE are enriched over MREE (La_n/Sm_n) and negatively correlate with enriched MREE over HREE values (Dy_n/Yb_n) in all samples. The vesicle filling calcite shows both positive and negative Ce/Ce* values between 0.75 and 1.41, the breccia calcite cement shows negative values between 0.18 and 0.92. Negative Ce anomalies are usually associated with oxidizing conditions producing Ce^{4+} instead of Ce^{3+} (e.g., Alibo and Nozaki, 1999). We observe positive to slightly negative Gd anomalies ($Gd/Gd^* = Gd_n/\mathrm{sqrt}(Eu_n \times Tb_n)$; Figure 4e). Positive Y_n/Ho_n anomalies are common (Figure 4f). Negative Ce/Ce* and Eu/Eu* anomalies together with higher Gd/Gd* and Y_n/Ho_n in the calcite cement of the volcanic breccia are interpreted to reflect a stronger influence of infiltrating seawater ($Ce/Ce^* = Ce_n/\mathrm{sqrt}(La_n \times Pr_n)$; $Eu/Eu^* = Eu_n/\mathrm{sqrt}(Sm_n \times Tb_n)$).

5 Discussion

5.1 Age data

Single-area ages overlap mostly within 2σ-errors per sample (Figure 3). Therefore, we interpret the calculated bulk sample age as a good approximation of the true age of calcite precipitation (Figure 4). No correlation between REE + Y content and U-Pb ages was found.

Calcite formation marks the phase of alkalinity-generating reactions in newly formed submarine volcanic rocks. Alkalinity describes the acid neutralizing capacity by formation of alkali and alkaline earth metal ion species during rock weathering (e.g., Spivack and Staudigel, 1994). This is crucial for interpreting calcite U-Pb ages. Possible high temperature hydrothermal alteration is restricted to discrete zones, such as veins, shear zones, and hydrothermal upflow zones (Harlov and Austrheim, 2013; Honnorez, 2003). It changes the mineral composition completely, such that primary igneous textures are obliterated (e.g. epidosites, Honnorez, 2003). Such rock types must be avoided as they are unlikely to reproduce related to OFA. By dating isolated calcite, far from hydrothermal upflow zones, we determine the age range of OFA occurring shortly after rock consolidation. This gives a first order minimum age estimate for ocean floor formation, if not the actual age of formation.

https://doi.org/10.5194/gchron-2021-27
Preprint. Discussion started: 20 September 2021

We note that, despite inter-sample variations, calcite ages are consistent with published radiometric ages in the North Pamir arc, including two hornblende $^{40}Ar/^{39}Ar$ ages of ~350 Ma from a meta-andesite, zircon U-Pb ages of ~329 Ma from felsic to intermediate volcanics in Altyn Darya valley (Schwab *et al.*, 2004), and zircon U-Pb ages of ~360 to 314 Ma from island arc granites (Ji et al., 2018; Rembe et al., 2021) (Figure 5).

5.2 Calcite REE + Y geochemistry

The hosting basalt has a flat C1-normalized REE pattern (Boynton, 1984), implying an intra-oceanic arc origin (Jiang et al., 2008; Rembe et al., 2021). We suggest a possible control of the basalt geochemistry on calcite REE patterns; any process altering this signal would significantly change the calcite REE pattern (Debruyne et al., 2016).

REE partition coefficients between aqueous solution and precipitating calcite have been studied experimentally (e.g., Perry and Gysi, 2018; Voigt et al., 2017). Evidently, variable physicochemical conditions lead to strongly differing integration of rare earth elements into the calcite lattice. We show that calcite cements of samples 17NP436a and b are distinguishable from vesicle fillings in samples 15NP233 and -236 (Figure 4e, f).

Calcite must be the major REE + Y sink as our samples do not show any intergrowing, co-precipitated mineral phase. The dominance of calcite hints at precipitation from CO_2-rich seawater derived hydrothermal fluids under low temperature conditions (Talbi and Honnorez, 2003; Honnorez, 2003). This happened in the upper few 100 meters of the oceanic crust. We assume a low mineralization temperature. Under this condition, Eu is trivalent and negative Eu/Eu* is directly inherited from the fluid reservoir (Debruyne et al., 2016). Pronounced negative Ce/Ce* values are a typical inherited signal of oxidizing seawater (e.g., Alibo and Nozaki, 1999); in correlation with increasing Y_n/Ho_n values, they trace back to oxidative sorption by Fe-Mn O(OH) species (Debruyne et al., 2016). Positive Gd/Gd* values may be interpreted as a seawater signal (e.g., Baar et al., 1985). However, markedly positive Gd anomalies together with positive Y_n/Ho_n values are less commonly reported. Similar features were observed for high salinity waters of the Jordan graben lakes (e.g., Möller et al., 2007). Because ocean floor aquifer porosities are highly heterogenous (e.g., Fisher and Becker, 2000), the higher porosity of volcanic breccias 17NP436a/b may have promoted seawater infiltration, leading to lower REE concentrations and more pronounced Ce/Ce*, Eu/Eu*, Gd/Gd* and Y_n/Ho_n anomalies compared to amygdaloidal basalt samples.

5.3 Implications on tectonic models of the Pamir

The results from petrological thin section examination, showing primary calcite fabrics, together with LA-ICP-MS trace element geochemistry, which reflect sea water infiltration, typical for OFA, are major arguments for preserved, primary U-Pb isotopic ratios. Our studies constrain the arc volcanic rocks in the NE Pamir to Carboniferous (Figure 5), significantly younger than correlative lithologies in the West Kunlun, which are dated to the Cambrian (e.g. Yixieke dacite, Xiao et al. (2005), Kudi ophiolite, Wang et al. (2021)). The results carry significant implications for the interpretation of Mesozoic and Cenozoic geodynamic evolution of the Tibet-Pamir orogen. Since the pioneering works of Burtman et al. (1963), Burtman and Molnar (1993), Pan (1994), Mattern et al. (1996), Xiao et al. (2002) and references therein, the Kudi-Oytag suture, or the "Paleozoic suture",

https://doi.org/10.5194/gchron-2021-27
Preprint. Discussion started: 20 September 2021

has been hypothesized to be a single, once continuous, E-W-striking feature that was bent towards the north by Cenozoic indentation of the Pamir into a postulated Tarim-Tajik block.

Recent publications outline an early Paleozoic history of the West Kunlun arc magmatism (Figure 6a). The southward subduction of the Proto-Tethys started in the Terreneuvian, dated by the 531 Ma Nanpingxueshan pluton in the Tianshuihai Group (Yin et al., 2020). As a consequence of the development of the Yixieke volcanic arc (Xiao et al., 2005) and the Yierba arc, the South Kunlun was intruded by the Yierba adakitic diorite at ca. 513 Ma (Yin et al., 2020). In response to slab roll-back, the Kudi ophiolite formed in a back-arc position between 513-516 Ma (Wang et al., 2021). The Proto-Tethys closed in the Silurian between 431-420 Ma (Wang et al., 2020) with exhumation of metamorphic units starting from ca. 440 Ma, as dated by monazite U-Pb from the Saitula Group (Zhang et al., 2018a). Closure of the Proto-Tethys was followed by the intrusion of A-type post-orogenic granites, dated as 420-405 Ma by zircon U-Pb in the North Kudi granite (Yuan et al., 2002; Liu et al., 2014).

However, corresponding, early Paleozoic geologic events or rock records in the North Pamir have not been reported. Instead, previous works on mafic to intermediate volcanic rocks and granitoids of the North Pamir show major, subduction related, arc magmatic activity in the mid to late Carboniferous (Rembe et al., 2021; Jiang et al., 2008; Ji et al., 2018; Kang et al., 2015). Carboniferous arc magmatic rocks found in the Waqia (Tang et al., 2020) and East Mazar (Li et al., 2006) tectonic slivers, reflect the closure of a remnant ocean basin, whereas major arc magmatic activity was focused on the North Pamir arc further to the west (Figure 6b). Stratigraphic relations and hiati point to a soft collision and obduction of that North Pamir arc in the early Permian (Rembe et al., 2021). No broad Paleozoic magmatic activity younger than Lower Devonian is known in the West Kunlun. The Carboniferous North Pamir arc granitoids intrude largely into poorly dated mafic volcanic rocks. Our calcite U-Pb ages agree with the only known ages of this volcanic unit from Schwab et al. (2004) (Figure 5). They corroborate the dissimilarity of the West Kunlun and North Pamir arc volcanic rocks, and therefore argue against the existence of a continuous Paleozoic suture extending from the Pamir to the West Kunlun.

6 Conclusion

Calcite hosted by Paleozoic ocean floor volcanic rocks was dated by LA-ICP-MS, yielding consistent Carboniferous ages. These ages agree with existing radiometric ages of volcanic units in the North Pamir, implying the presence of Mississippian oceanic crust in the North Pamir. This finding argues against models invoking a continuous, early Paleozoic Kunlun belt, stretching from the West Kunlun far into the North Pamir. REE + Y geochemistry of our samples indicates a mixture of at least two geochemical reservoirs—the basaltic rock being leached by interaction with seawater and the seawater itself. We interpret REE + Y variations among samples in the same unit as effects of variable porosities. Low trace element concentration and anomalies typically associated with oxidizing seawater occur when porosity is high, arguing for a high water-rock ratio. In this study, REE + Y variability did not influence U-Pb age data.

Our work demonstrates the importance of textural and geochemical data in interpreting calcite U-Pb ages. We show, that calcite U-Pb dating has great potential in constraining the age of oceanic crust, which is usually difficult to date radiometrically.

https://doi.org/10.5194/gchron-2021-27
Preprint. Discussion started: 20 September 2021

7 Appendices

Appendix A: Reflected light images, Fig.A1–A4

Appendix B: X-ray fluorescence microscopy (XFM) maps, Fig. B1–6

Appendix C: Tera–Wasserburg plot of each ablation area, Fig.C1a–d

Appendix D: REE data of each ablation area, Fig.D1

8 Code and data availability

Whole rock geochemistry data used from literature (Rembe et al. (2021), S1) as well as LA-ICP-MS isotope data (S2) and geochemistry (S3) will be uploaded to UQ eSpace (https://espace.library.uq.edu.au/), run by the University of Queensland, upon acceptance.

9 Author contribution

JR, RZ, ERS, and JK conceptualized the project. Fieldwork was carried out by JR, ERS, JK, and CJ. Methodological concept preparation, Laboratory work and data interpretation was done by RZ, JR, JXZ, YF, and DLH. JR prepared a first draft of the manuscript and all authors contributed to the review and editing procedure.

10 Competing interests

All authors declare that they do not have any conflict of interest.

11 Acknowledgement

We thank Langtao Liu for help with field work, and Antje Musiol and Baiansuluu Terbishalieva for support with laboratory work at the University of Potsdam.

12 Funding statement

The project was funded by Deutsche Forschungs Gesellschaft e.V. (DFG) grant SO 436/12-1 to Sobel and DFG grant KL 495/27-1 to Kley. Additional support was provided by grants to Sobel, Zhao and Zhou through the Australia-Germany Joint Research Cooperation Scheme, and to Howard and Zhou through the Australian Synchrotron Access Program. Jie was supported by grants through the 2nd Tibetan Plateau Scientific Expedition and Research Program (STEP, 2019QZKK0901) and State Key Lab. of Earthquake Dynamics of China (LED2016A05).

https://doi.org/10.5194/gchron-2021-27
Preprint. Discussion started: 20 September 2021

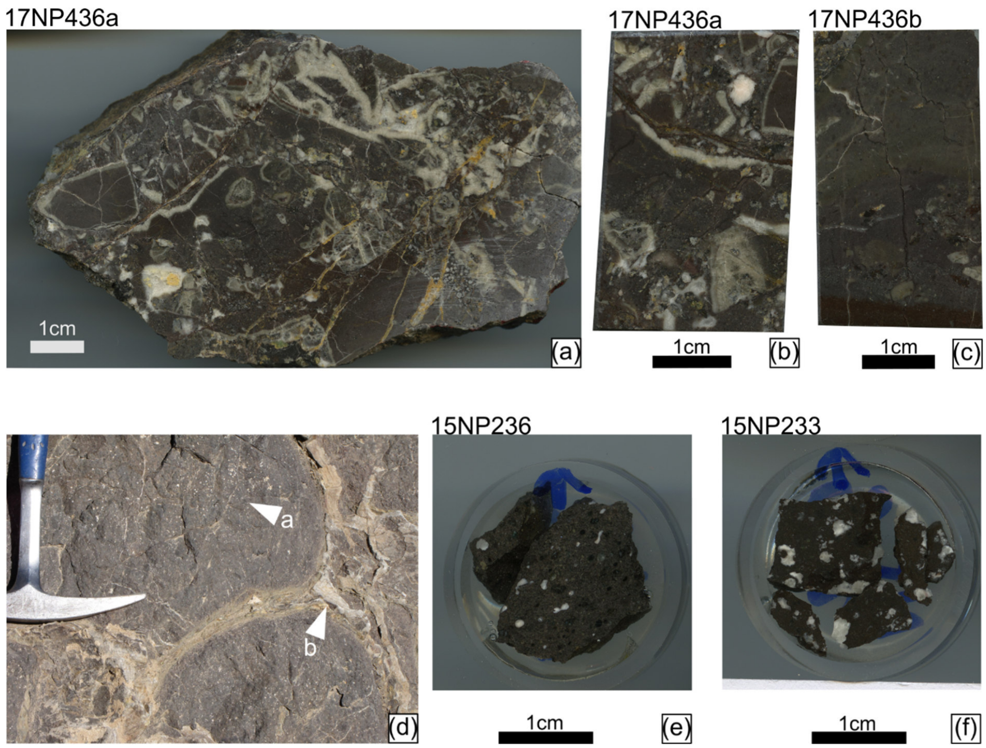

Figure 1: Sample photographs of hand specimen of sample 17NP436a (a) and polished rock block used for LA-ICP-MS measurements of sample 17NP436a (b) and 17NP436b (c). Field photograph of amygdaloidal pillow-basalts in Qimgan valley (d), with white arrows pointing at calcite filled vesicles (arrow a) and massive interstitial calcite (arrow b). Polished rock specimen 15NP236 (e) and 15NP233 (f) of similar rocks, were used for LA-ICP-MS.

https://doi.org/10.5194/gchron-2021-27
Preprint. Discussion started: 20 September 2021

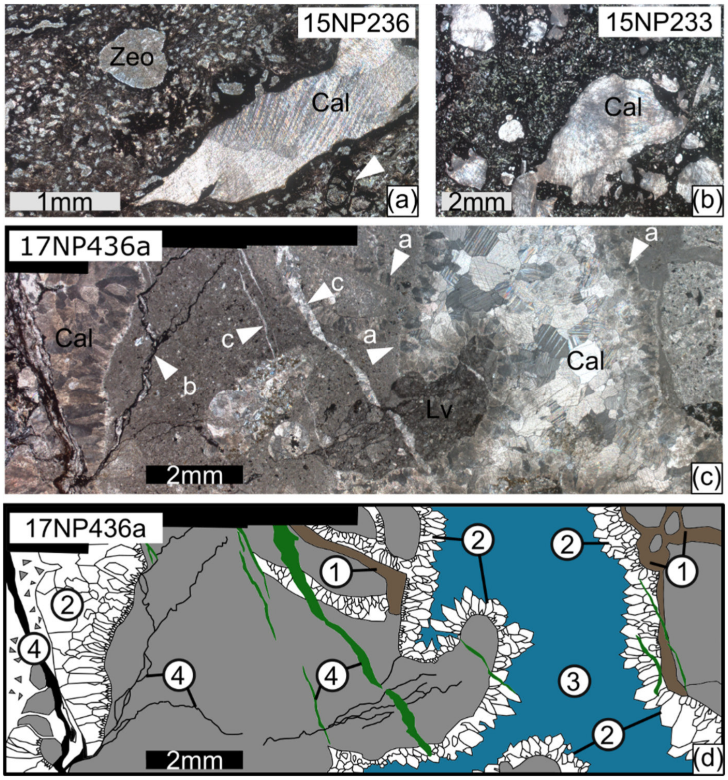

Figure 2: Typical calcite filled vesicles of sample 15NP236 (a), in this case with spary calcite and zeolite mineralization. The white arrow marks preserved perlitic structures. Botryoidal calcite was found in both amygdaloid-basalt samples, the example in (b) is from 15NP233. Fig. 1c shows a thin section photograph of sample 17NP436a. White arrows indicate radial fibrous calcite (a), dark styloliths (b), calcite filled fissures (c). Fig. 1a, b, c under crossed polarized light. Fig. 1d shows a schematic sketch of microphotograph Fig. 1c, delineating a sequence of 4 events: (1) formation of hydrothermal clay, (2) precipitation of fibrous-radial calcite along the walls of brecciated volcanic rock fragments, (3) late-stage equant calcite formation, (4) pressure solution and formation of styloliths (dark lines) and reprecipitation of dissolved calcite in fissures (green). Areas 2 and 3 are targets for laser ablation.

https://doi.org/10.5194/gchron-2021-27
Preprint. Discussion started: 20 September 2021

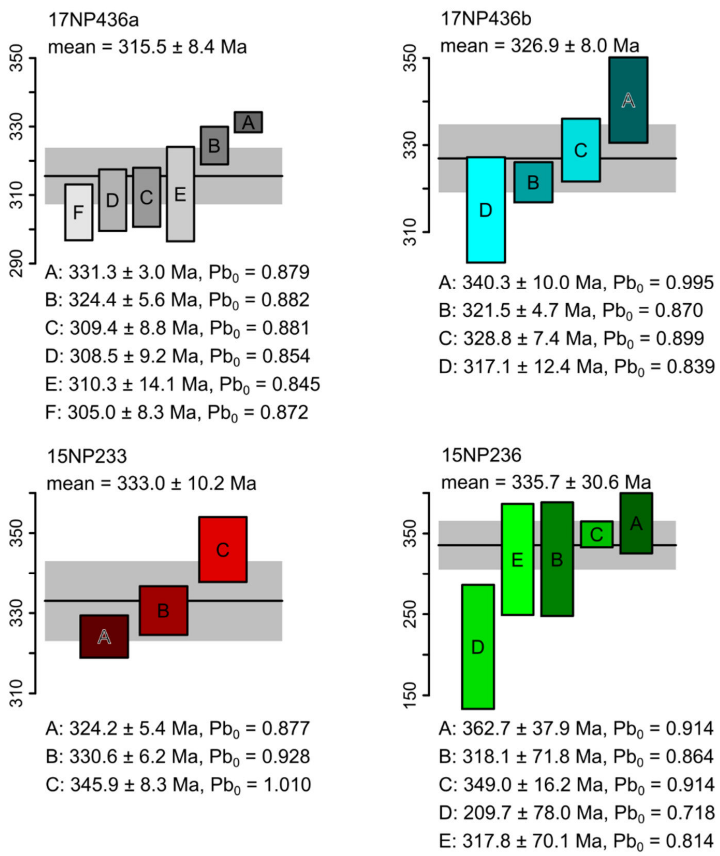

Figure 3: Intra sample age dispersion, age error bars are in ascending order. All errors are 2σ. Single ablation areas are color-coded and marked with capital letters. Exact locations on samples are shown in Appendix A.

https://doi.org/10.5194/gchron-2021-27
Preprint. Discussion started: 20 September 2021

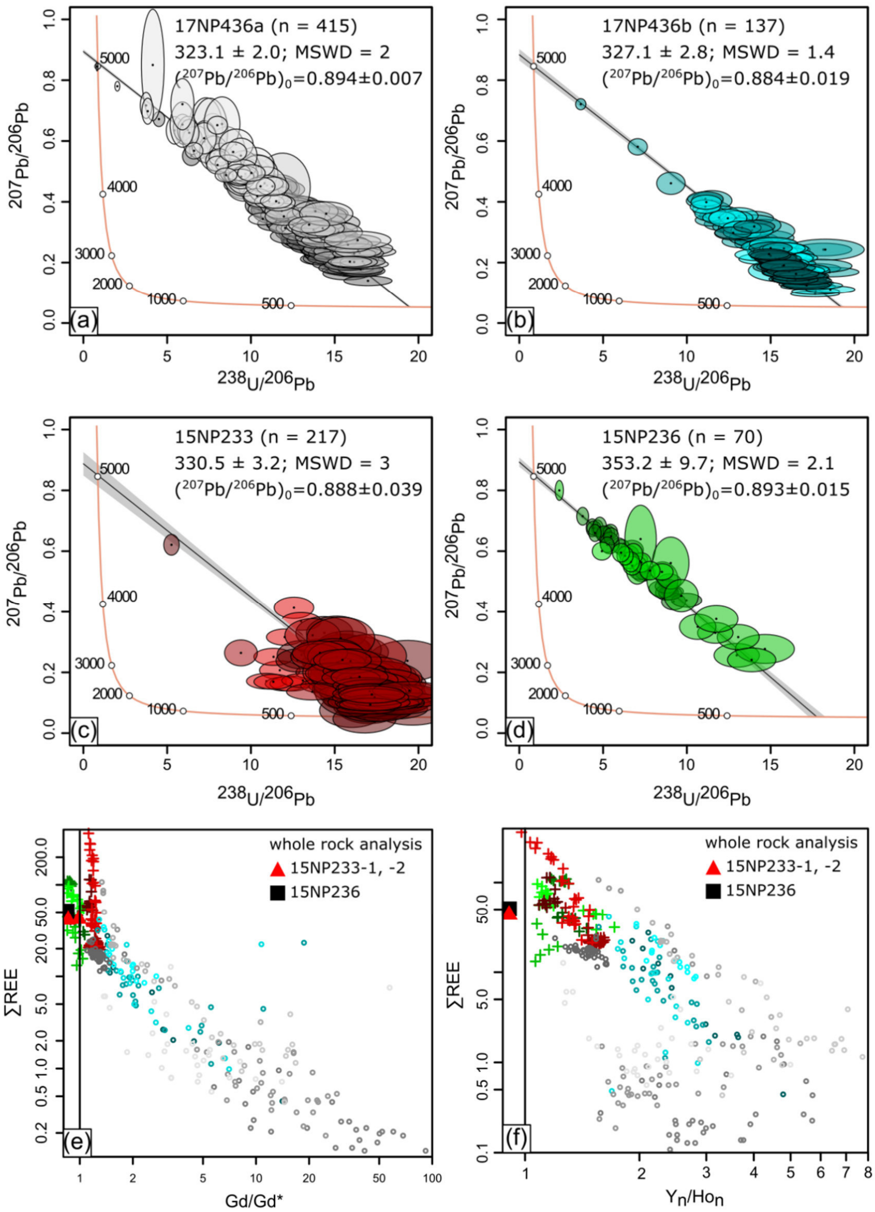

Figure 4: Plots of all Isotope ratios obtained from single ablation areas. Cemented volcanic breccia in samples 17NP436a and b (a, b) gave similar ages. Sample 15NP233 (c) has a higher dispersion. Sample 15NP236 (d) shows a good linear trend and a good fit. (e) Mixing trend between high total REE—negative Gd/Gd and low total REE—positive Gd/Gd* composition. (f) Higher Y_n/Ho_n values correlate with low total REE. Y and Ho normalized against chondrite values of Anders and Grevesse (1989). (e, f) + -15NP233, -236, **o** -17NP436A, -B; color-code see Fig. 2.*

https://doi.org/10.5194/gchron-2021-27
Preprint. Discussion started: 20 September 2021

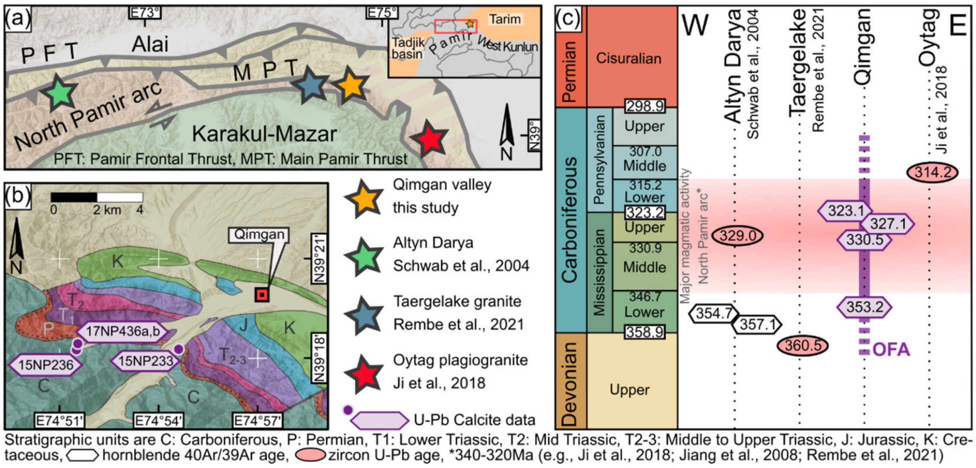

Figure 5: (a) Map of the northeastern Pamir with location of radiometric ages for the North Pamir arc volcanic rocks, shown in c. (b) Detailed field locations of samples in the Qimgan valley (map after Henan Institute of Geological Survey (2014)). There is a sedimentary hiatus between the Middle Pennsylvanian and the Guadalupian (Rembe et al., 2021). (c) Overview of selected literature data and newly obtained data for OFA of the North Pamir Carboniferous arc.

https://doi.org/10.5194/gchron-2021-27
Preprint. Discussion started: 20 September 2021

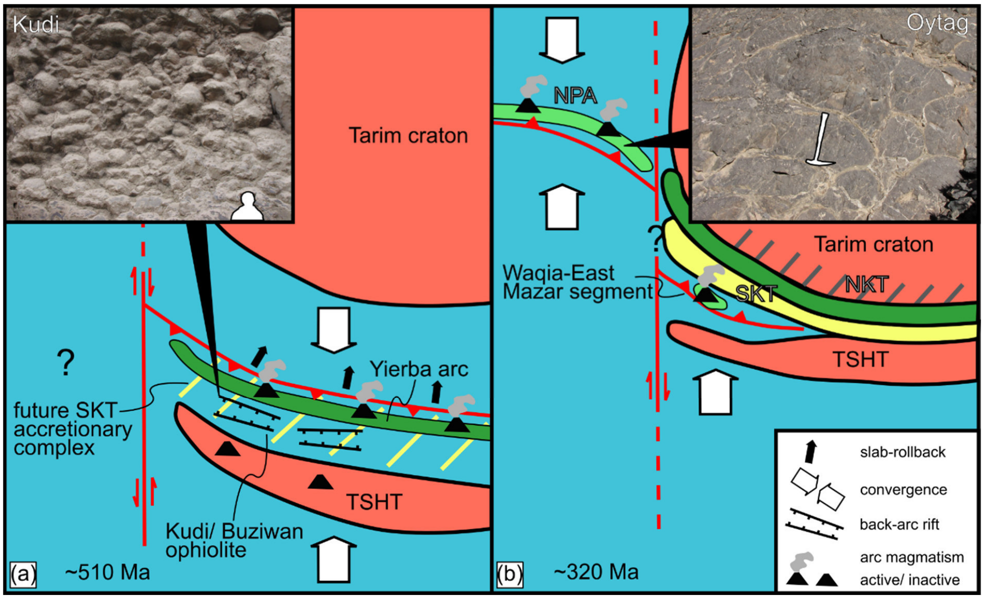

Figure 6: (a) Paleogeographic situation in the mid-Cambrian: The roll-back of the Proto-Tethys slab caused the formation of the Kudi ophiolite, exposed in the Buziwan valley (Wang et al., 2021). (b) Paleogeographic situation in the upper Mississippian: The North Pamir arc formed along an intra-oceanic subduction zone (Jiang et al., 2008) forming the Oytag segment in its eastern branch. Subduction related Waqia granite (Tang et al., 2020) and East Mazar granite (Li et al., 2006), both present as tectonic slivers, suggest the presence of a remnant oceanic basin between Tianshuihai and South Kunlun Terrane accretionary complex, as suggested by Zhang et al. (2018b). Small photographs show pillow basalts in the Kudi section (in a) and Oytag near Qimgan (in b). SKT-South Kunlun Terrane, TSHT-Tianshuihai Terrane, NPA-North Pamir volcanic arc, NKT-North Kunlun Terrane.

https://doi.org/10.5194/gchron-2021-27
Preprint. Discussion started: 20 September 2021

13 REFERENCES

Alibo, D. S. and Nozaki, Y.: Rare earth elements in seawater: particle association, shale-normalization, and Ce oxidation, Geochimica et Cosmochimica Acta, 63, 363–372, 1999.

Anders, E. and Grevesse, N.: Abundances of the elements: Meteoritic and solar, Geochimica et Cosmochimica Acta, 53, 197–214, 1989.

Baar, H. J. de, Brewer, P. G., and Bacon, M. P.: Anomalies in rare earth distributions in seawater: Gd and Tb, Geochimica et Cosmochimica Acta, 49, 1961–1969, https://doi.org/10.1016/0016-7037(85)90090-0, 1985.

Bazhenov, M. L. and Burtman, V. S.: The kinematics of the Pamir arc: Geotectonics, v. 16, 1982.

Boynton, W. V.: Cosmochemistry of the rare earth elements: meteorite studies, in: Developments in geochemistry, Elsevier, 63–114, 1984.

Burtman, V. S., Peive, A. V., and Ruzhentsev, S. V.: The main lateral faults of the Tien Shan and Pamir, Faults and Horizontal Movements of the Earth's Crust, 152–172, 1963.

Burtman, V. S. and Molnar, P. H.: Geological and geophysical evidence for deep subduction of continental crust beneath the Pamir, Geological Society of America, 1993.

Coogan, L. A. and Gillis, K. M.: Low-Temperature Alteration of the Seafloor: Impacts on Ocean Chemistry, Annu. Rev. Earth Planet. Sci., 46, 21–45, 2018.

Coogan, L. A., Parrish, R. R., and Roberts, N. M. W.: Early hydrothermal carbon uptake by the upper oceanic crust: Insight from in situ U-Pb dating, Geol, 44, 147–150, 2016.

Debruyne, D., Hulsbosch, N., and Muchez, P.: Unraveling rare earth element signatures in hydrothermal carbonate minerals using a source–sink system, Ore Geology Reviews, 72, 232–252, 2016.

Fisher, A. T. and Becker, K.: Channelized fluid flow in oceanic crust reconciles heat-flow and permeability data, Nature, 403, 71–74, 2000.

Godeau, N., Deschamps, P., Guihou, A., Leonide, P., Tendil, A., Gerdes, A., Hamelin, B., and Girard, J.-P.: U-Pb dating of calcite cement and diagenetic history in microporous carbonate reservoirs: Case of the Urgonian Limestone, France, Geology, 46, 247–250, 2018.

Gonzalez, L. A. and Carpente, S. J.: Inorganic Calcite Morphology: Roles of Fluid Chemistry and Fluid Flow, SEPM JSR, Vol. 62, 1992.

Harlov, D. E. and Austrheim, H. (Eds.): Metasomatism and the chemical transformation of rock: The role of fluids in terrestrial and extraterrestrial processes / Daniel E. Harlov, Håkon Austrheim [editors], Lecture notes in earth system sciences, 2193-8571, Springer, Heidelberg, London, 2013.

Heath, M., Phillips, D., and Matchan, E. L.: An evidence-based approach to accurate interpretation of 40Ar/39Ar ages from basaltic rocks, Earth and Planetary Science Letters, 498, 65–76, 2018.

Henan Institute of Geological Survey: The 1:250000 Geological Map of the Peoples Republic of China (J43C001002, Kuergan), China Coal Xi' and Map Printing Co., Ltd., 2014.

https://doi.org/10.5194/gchron-2021-27
Preprint. Discussion started: 20 September 2021

Honnorez, J.: Hydrothermal alteration vs. ocean-floor metamorphism. A comparison between two case histories: the TAG hydrothermal mound (Mid-Atlantic Ridge) vs. DSDP/ODP Hole 504B (Equatorial East Pacific), Comptes Rendus Geoscience, 335, 781–824, 2003.

Howard, D. L., Jonge, M. D. de, Afshar, N., Ryan, C. G., Kirkham, R., Reinhardt, J., Kewish, C. M., McKinlay, J., Walsh, A., and Divitcos, J.: The XFM beamline at the Australian Synchrotron, Journal of Synchrotron Radiation, 27, 1447–1458, 2020.

Ji, W. H., Chen, S. J., Li, R. S., He, S. P., Zhao, Z. M., and Pan, X. P.: The origin of Carboniferous-Permian magmatic rocks in Oytag area, West Kunlun: Back-arc basin?, Acta Petrologica Sinica, 34, 2393–2409, 2018.

Jiang, Y.-H., Liao, S.-Y., Yang, W.-Z., and Shen, W.-Z.: An island arc origin of plagiogranites at Oytag, western Kunlun orogen, northwest China: SHRIMP zircon U–Pb chronology, elemental and Sr–Nd–Hf isotopic geochemistry and Paleozoic tectonic implications, Lithos, 106, 323–335, https://doi.org/10.1016/j.lithos.2008.08.004, 2008.

Kang, L., Xiao, P. X., Gao, X. F., Wang, C., Yang, Z. C., and Xi, R. G.: Geochemical characteristics, petrogenesis and tectonic setting of oceanic plagiogranites belt in the northwestern margin of western Kunlun, Acta Petrologica Sinica, 31, 2566–2582, 2015.

Li, B., Yao, J., Ji, W. H., Zhang, J., Yin, Z., Chen, G., Lin, X., Zhang, Q., KONG, W., Wang, F., and LIU, X.: Characteristics and zircon SHRIMP U-Pb ages of the arc magmatic rocks in Mazar, southern Yecheng, West Kunlun Mountains., Geological Bulletin of China, Z1, 124–132, 2006.

Liu, Z., Jiang, Y.-H., Jia, R.-Y., Zhao, P., Zhou, Q., Wang, G.-C., and Ni, C.-Y.: Origin of Middle Cambrian and Late Silurian potassic granitoids from the western Kunlun orogen, northwest China: a magmatic response to the Proto-Tethys evolution, Miner Petrol, 108, 91–110, 2014.

Mattern, F., Schneider, W., Li, Y., and Li, X.: A traverse through the western Kunlun (Xinjiang, China): Tentative geodynamic implications for the Paleozoic and Mesozoic, Geol Rundsch, 85, 705–722, 1996.

Möller, P., Rosenthal, E., Geyer, S., Guttman, J., Dulski, P., Rybakov, M., Zilberbrand, M., Jahnke, C., and Flexer, A.: Hydrochemical processes in the lower Jordan valley and in the Dead Sea area, Chemical Geology, 239, 27–49, 2007.

Nuriel, P., Craddock, J., Kylander-Clark, A. R. C., Uysal, I. T., Karabacak, V., Dirik, R. K., Hacker, B. R., and Weinberger, R.: Reactivation history of the North Anatolian fault zone based on calcite age-strain analyses, Geology, 47, 465–469, 2019.

Pan, Y.: Discovery and evidence of the fifth suture zone of Qinghai-xizang plateau, Chinese Journal of Geophysics, 2, 1994.

Paton, C., Hellstrom, J., Paul, B., Woodhead, J., and Hergt, J.: Iolite: Freeware for the visualisation and processing of mass spectrometric data, Journal of Analytical Atomic Spectrometry, 26, 2508–2518, 2011.

Perry, E. P. and Gysi, A. P.: Rare Earth Elements in Mineral Deposits: Speciation in Hydrothermal Fluids and Partitioning in Calcite, Geofluids, 2018, 1–19, https://doi.org/10.1155/2018/5382480, available at: https://www.hindawi.com/journals/geofluids/2018/5382480/, 2018.

Pringle, M. S.: Age Progressive Volcanism in the Musicians Seamounts: A Test of the Hot Spot Hypothesis for the Late Cretaceous Pacific, in: The Mesozoic Pacific: Geology, Tectonics, and Volcanism, American Geophysical Union (AGU), 187–215, https://doi.org/10.1029/GM077p0187, 2013.

Rasbury, E. T., Present, T. M., Northrup, P., Tappero, R. V., Lanzirotti, A., Cole, J. M., Wooton, K. M., and Hatton, K.: Tools for uranium characterization in carbonate samples: case studies of natural U–Pb geochronology reference materials, Geochronology, 3, 103–122, https://doi.org/10.5194/gchron-3-103-2021, 2021.

Rembe, J., Sobel, E. R., Kley, J., Zhou, R., Thiede, R., and Chen, J.: The Carboniferous Arc of the North Pamir, Lithosphere, 2021, https://doi.org/10.2113/2021/6697858, available at: https://pubs.geoscienceworld.org/gsa/lithosphere/article/2021/1/6697858/594514/The-Carboniferous-Arc-of-the-North-Pamir, 2021.

Roberts, N. M. W., Žák, J., Vacek, F., and Sláma, J.: No more blind dates with calcite: Fluid-flow vs. fault-slip along the Očkov thrust, Prague Basin, Geoscience Frontiers, 12, 101143, 2021.

Roberts, N. M. W., Rasbury, E. T., Parrish, R. R., Smith, C. J., Horstwood, M. S. A., and Condon, D. J.: A calcite reference material for LA-ICP-MS U-Pb geochronology, Geochemistry, Geophysics, Geosystems, 18, 2807–2814, https://doi.org/10.1002/2016GC006784, available at: http://onlinelibrary.wiley.com/doi/10.1002/2016GC006784/full, 2017.

Schwab, M., Ratschbacher, L., Siebel, W., McWilliams, M., Minaev, V., Lutkov, V., Chen, F., Stanek, K., Nelson, B., Frisch, W., and Wooden, J. L.: Assembly of the Pamirs: Age and origin of magmatic belts from the southern Tien Shan to the southern Pamirs and their relation to Tibet, Tectonics, 23, n/a-n/a, https://doi.org/10.1029/2003TC001583, 2004.

Spivack, A. J. and Staudigel, H.: Low-temperature alteration of the upper oceanic crust and the alkalinity budget of seawater, Chemical Geology, 115, 239–247, 1994.

Staudigel, H., Plank, T., White, B., and Schmincke, H.-U.: Geochemical Fluxes During Seafloor Alteration of the Basaltic Upper Oceanic Crust: DSDP Sites 417 and 418, in: Subduction top to bottom, edited by: Bebout, G. E., Scholl, D. W., and Kirby, S. H., American Geophysical Union, Washington, 19–38, https://doi.org/10.1029/GM096p0019, 2013.

Su, A., Chen, H., Feng, Y., Zhao, J., Nguyen, A. D., Wang, Z., and Long, X.: Dating and characterizing primary gas accumulation in Precambrian dolomite reservoirs, Central Sichuan Basin, China: Insights from pyrobitumen Re-Os and dolomite U-Pb geochronology, Precambrian Research, 350, 105897, 2020.

Talbi, E. H. and Honnorez, J.: Low-temperature alteration of mesozoic oceanic crust, Ocean Drilling Program Leg 185, Geochem. Geophys. Geosyst., 4, 2003.

Tang, W., Wang, S., Liu, Y., Yao, X., and Li, M.: Origin of Carboniferous intra-oceanic arc granitoids from the eastern Pamir and implications for the Paleo-Tethyan ocean, 2020.

Vanghi, V., Borsato, A., Frisia, S., Howard, D. L., Gloy, G., Hellstrom, J., and Bajo, P.: High-resolution synchrotron X-ray fluorescence investigation of calcite coralloid speleothems: Elemental incorporation and their potential as environmental archives, Sedimentology, 66, 2661–2685, 2019.

https://doi.org/10.5194/gchron-2021-27
Preprint. Discussion started: 20 September 2021

Voigt, M., Mavromatis, V., and Oelkers, E. H.: The experimental determination of REE partition coefficients in the water-calcite system, Chemical Geology, 462, 30–43, 2017.

Waagstein, R., Guise, P., and Rex, D.: K/Ar and 39 Ar/ 40 Ar whole-rock dating of zeolite facies metamorphosed flood basalts: the upper Paleocene basalts of the Faroe Islands, NE Atlantic, Geological Society, London, Special Publications, 197, 219–252, https://doi.org/10.1144/GSL.SP.2002.197.01.09, 2002.

Wang, P., Zhao, G., Liu, Q., Han, Y., Zhang, Y., Yao, J., and Yu, S.: Slab-controlled progressive evolution of the Kudi back-arc ophiolite in response to the rollback of the Proto-Tethys oceanic slab, in Western Kunlun, NW Tibetan Plateau, Lithos, 380-381, 105877, 2021.

Wang, P., Zhao, G., Han, Y., Liu, Q., Yao, J., Yu, S., and Li, J.: Timing of the final closure of the Proto-Tethys Ocean: Constraints from provenance of early Paleozoic sedimentary rocks in West Kunlun, NW China, Gondwana Research, 2020.

Woodhead, J. D. and Hergt, J. M.: Strontium, neodymium and lead isotope analyses of NIST glass certified reference materials: SRM 610, 612, 614, Geostandards Newsletter, 25, 261–266, 2001.

Xiao, W. J., Windley, B. F., Liu, D. Y., Jian, P., Liu, C. Z., Yuan, C., and Sun, M.: Accretionary tectonics of the Western Kunlun Orogen, China: A Paleozoic–Early Mesozoic, long-lived active continental margin with implications for the growth of Southern Eurasia, The Journal of Geology, 113, 687–705, 2005.

Xiao, W. J., Windley, B. F., Chen, H. L., Zhang, G. C., and Li, J. L.: Carboniferous-Triassic subduction and accretion in the western Kunlun, China: Implications for the collisional and accretionary tectonics of the northern Tibetan Plateau, Geology, 30, 295–298, 2002.

Yang, P., Wu, G., Nuriel, P., Nguyen, A. D., Chen, Y., Yang, S., Feng, Y., Ren, Z., and Zhao, J.: In situ LA-ICPMS UPb dating and geochemical characterization of fault-zone calcite in the central Tarim Basin, northwest China: Implications for fluid circulation and fault reactivation, Chemical Geology, 568, 120125, 2021.

Yin, J., Xiao, W., Sun, M., Chen, W., Yuan, C., Zhang, Y., Wang, T., Du, Q., Wang, X., and Xia, X.: Petrogenesis of Early Cambrian granitoids in the western Kunlun orogenic belt, Northwest Tibet: Insight into early stage subduction of the Proto-Tethys Ocean, Bulletin, 132, 2221–2240, 2020.

Yuan, C., Sun, M., Zhou, M., Zhou, H., Xiao, W., and Li, J.: Tectonic Evolution of the West Kunlun: Geochronologic and Geochemical Constraints from Kudi Granitoids, International Geology Review, 44, 653–669, https://doi.org/10.2747/0020-6814.44.7.653, 2002.

Zhang, C.-L., Zou, H.-B., Ye, X.-T., and Chen, X.-Y.: Tectonic evolution of the West Kunlun Orogenic Belt along the northern margin of the Tibetan Plateau: Implications for the assembly of the Tarim terrane to Gondwana, Geoscience Frontiers, 2018a.

Zhang, C.-L., Zou, H.-B., Ye, X.-T., and Chen, X.-Y.: Tectonic evolution of the NE section of the Pamir Plateau: New evidence from field observations and zircon U-Pb geochronology, Tectonophysics, 723, 27–40, 2018b.

https://doi.org/10.5194/gchron-2021-27
Preprint. Discussion started: 20 September 2021

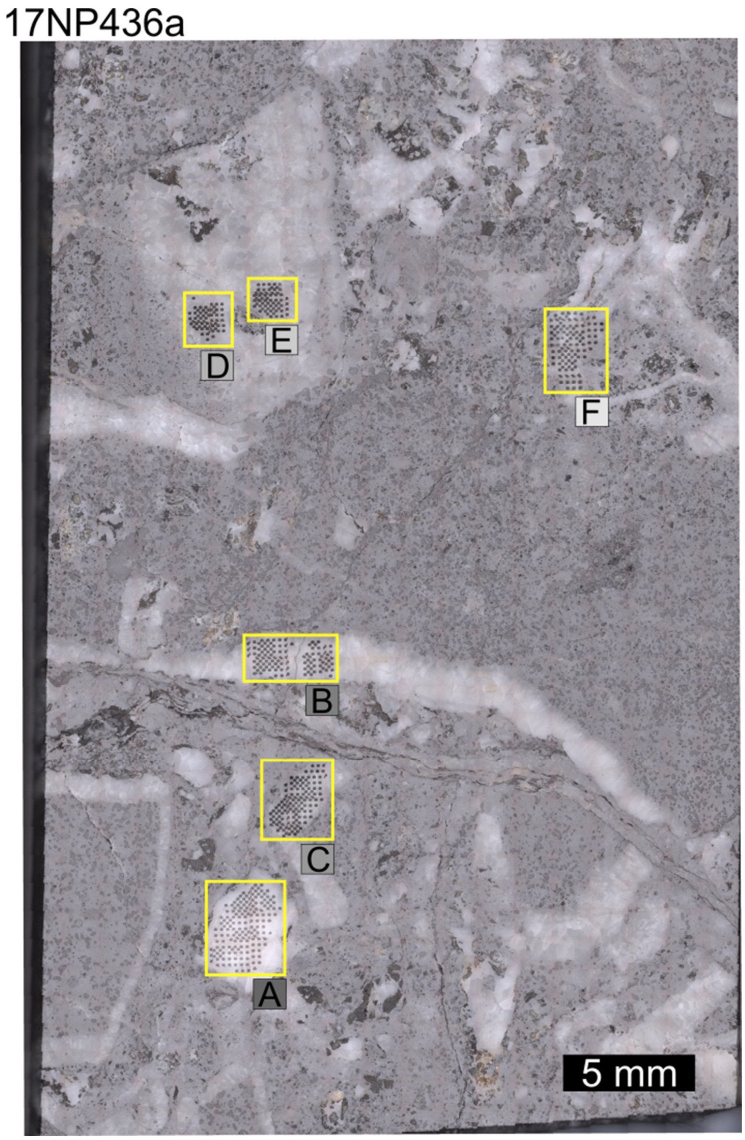

Figure A1. Reflected light image of sample 17NP436a with marked ablation areas. Letter, attached to the yellow boxes, appended to the sample name, labels the ablation areas. Colors of label boxes are consistent with colors of in-text figures.

https://doi.org/10.5194/gchron-2021-27
Preprint. Discussion started: 20 September 2021

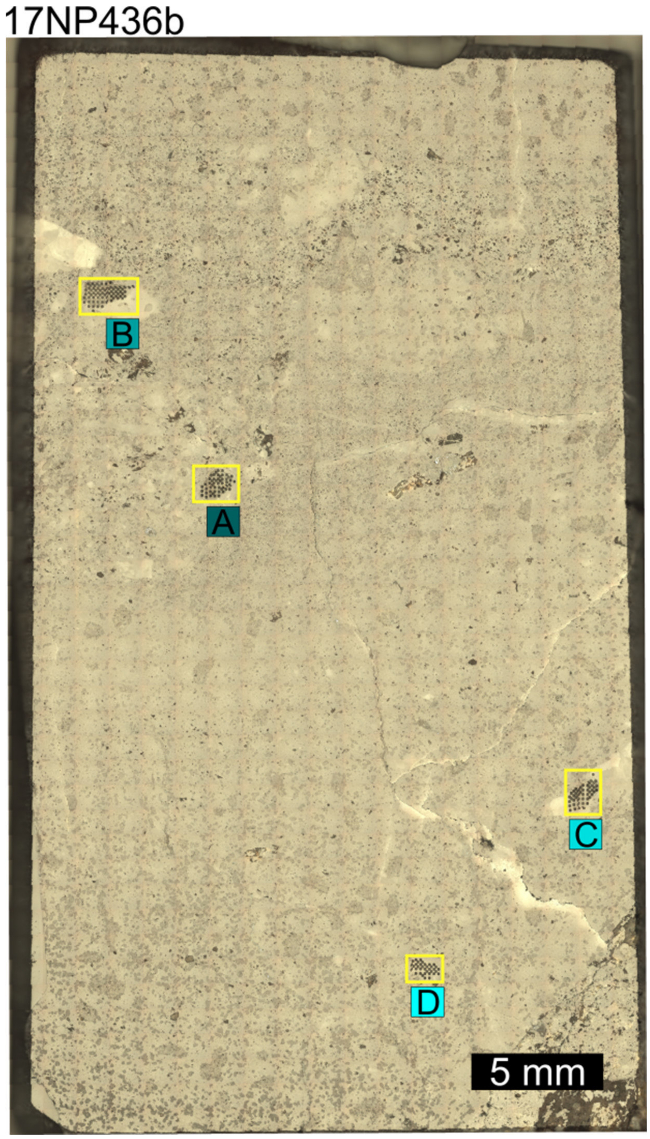

Figure A2. Reflected light image of sample 17NP436b with marked ablation areas. Letter, attached to the yellow boxes, appended to the sample name, labels the ablation areas. Colors of label boxes are consistent with colors of in-text figures.

https://doi.org/10.5194/gchron-2021-27
Preprint. Discussion started: 20 September 2021

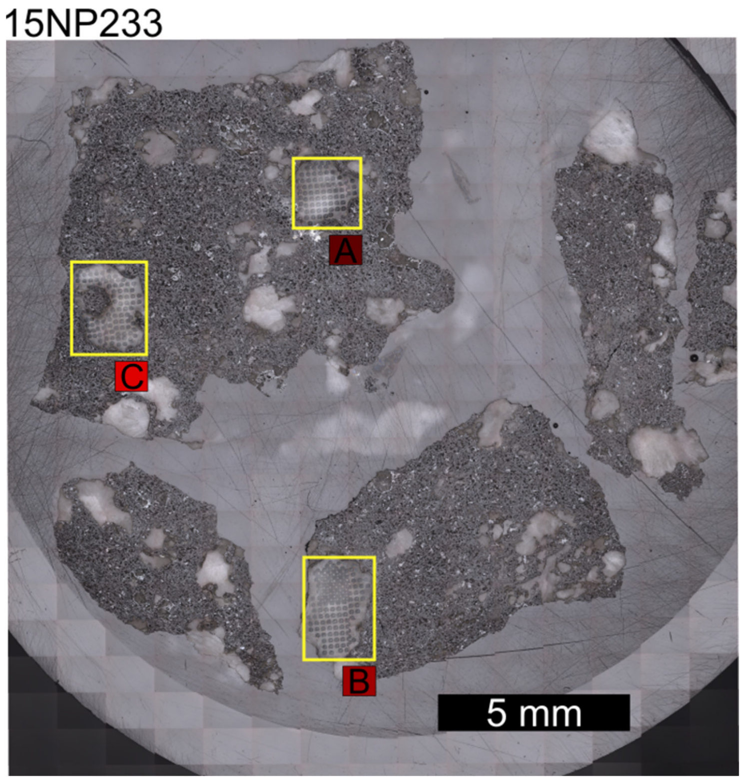

Figure A3. Reflected light image of sample 15NP233 with marked ablation areas. Letter, attached to the yellow boxes, appended to the sample name, labels the ablation areas. Colors of label boxes are consistent with colors of in-text figures.

https://doi.org/10.5194/gchron-2021-27
Preprint. Discussion started: 20 September 2021

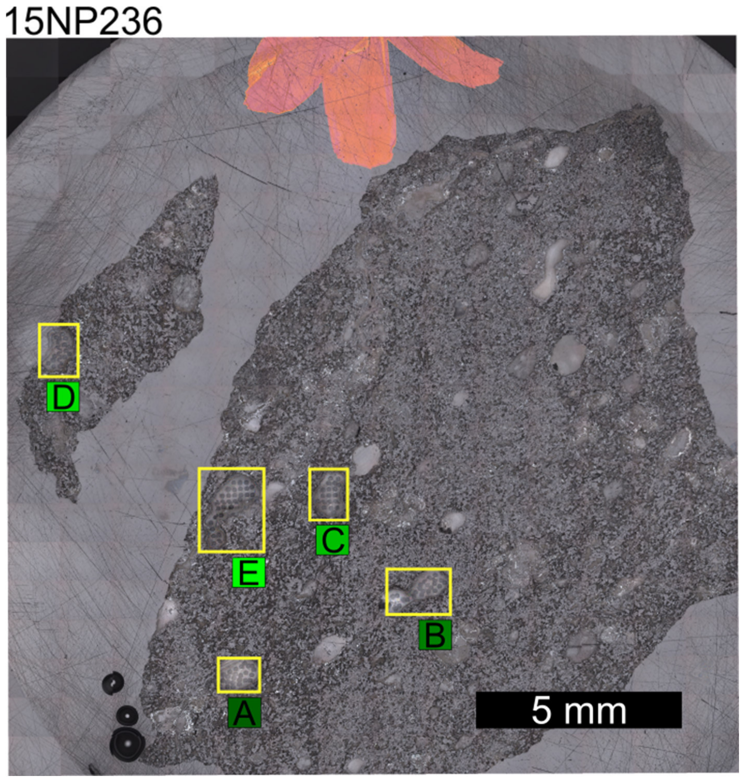

Figure A4. Reflected light image of sample 15NP236 with marked ablation areas. Letter, attached to the yellow boxes, appended to the sample name, labels the ablation areas. Colors of label boxes are consistent with colors of in-text figures.

https://doi.org/10.5194/gchron-2021-27
Preprint. Discussion started: 20 September 2021

Reflective light photo

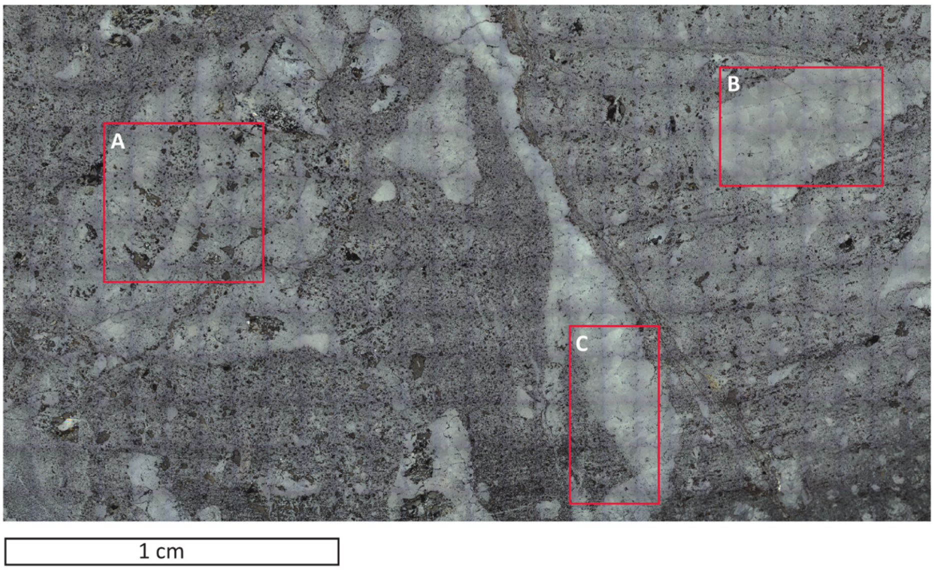

Cross-polarized light photo

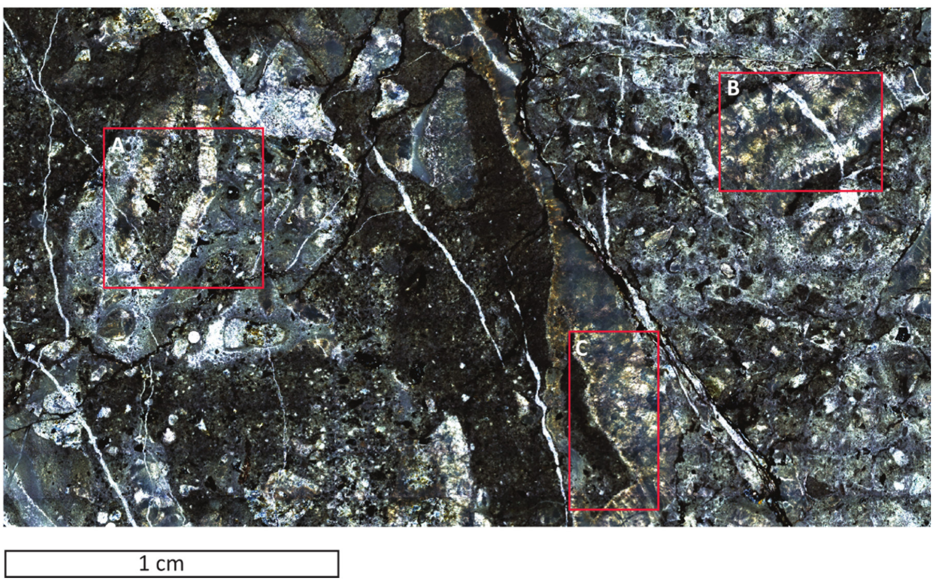

Figure B1. Reflected light image and cross-polarized light image of the investigation area on sample 17NP436a.

https://doi.org/10.5194/gchron-2021-27
Preprint. Discussion started: 20 September 2021

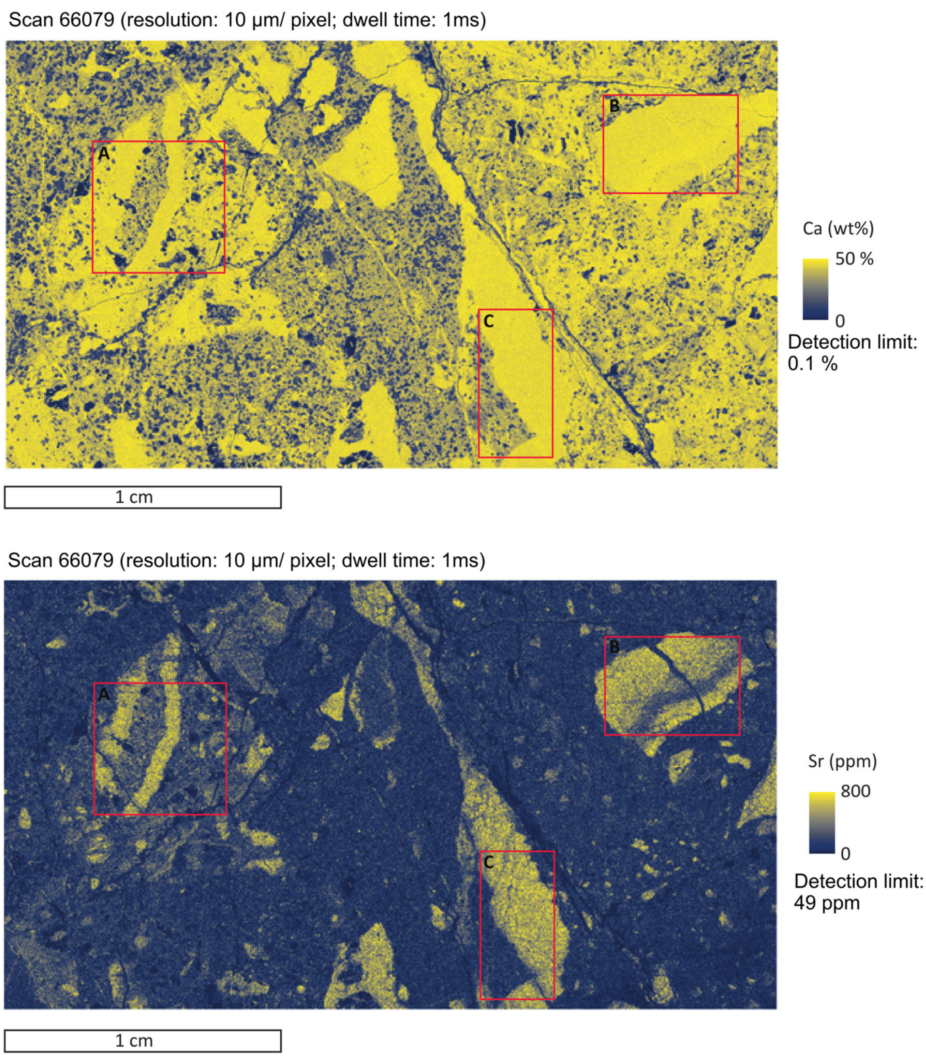

Figure B2. Coarse scan of the investigation areas on sample 17NP436a for Ca and Sr.

Area A shows a rock fragment fringed by radial-fibrous calcite cement. The right fissure shows calcite growing from both walls toward the center, showing lower Sr values in the center of the vein.

Area B shows an isolated fragment of radial-fibrous to equant cement with Sr and Ca zoning. High Sr/ low Ca values occur in the radial-fibrous calcite along the lower-right boundary with an abrupt change to low Sr/ high Ca values in the center that grade into high Sr/ low Ca values in a broad zone along the upper-left boundary. The low Sr/ high Ca values occur at the transition from radial-fibrous to equant calcite crystals. A younger calcite filled fissure crosscuts the calcite cement fragment. Crucial are the much lower Sr values. This fissure formed during tectonic straining of the rock, pressure solution and reprecipitation of calcite.

Area C shows calcite crystals with highest Sr/ lowest Ca values in the center of the single crystals.

https://doi.org/10.5194/gchron-2021-27
Preprint. Discussion started: 20 September 2021

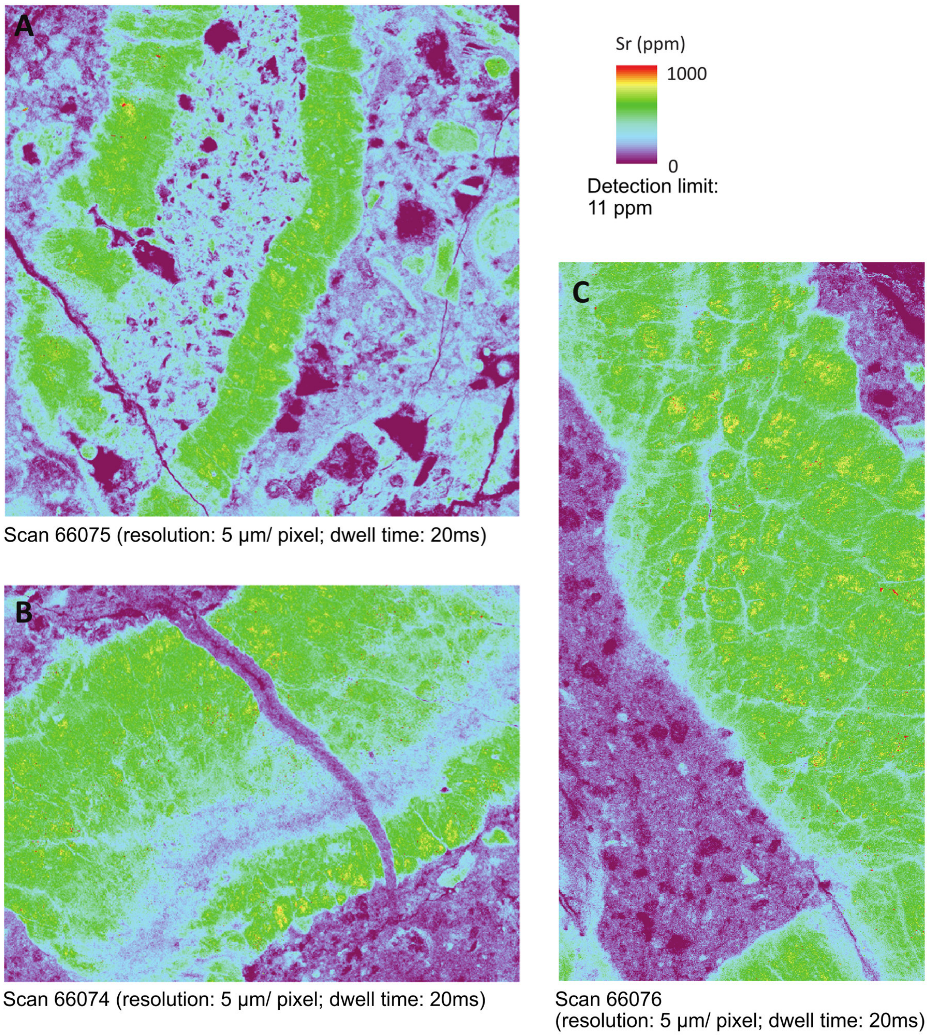

Figure B3. Fine scan of the investigation areas on sample 17NP436a for Sr.

https://doi.org/10.5194/gchron-2021-27
Preprint. Discussion started: 20 September 2021

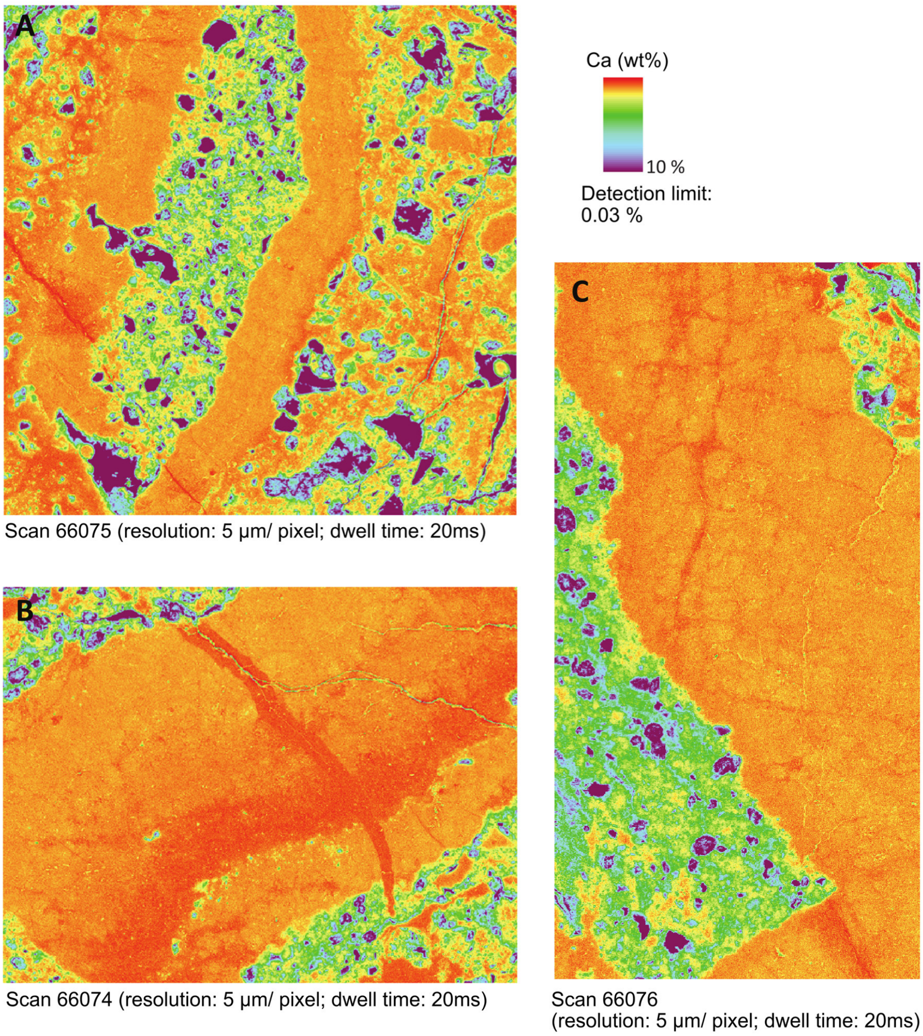

Figure B4. Fine scan of the investigation areas on sample 17NP436a for Ca.

https://doi.org/10.5194/gchron-2021-27
Preprint. Discussion started: 20 September 2021

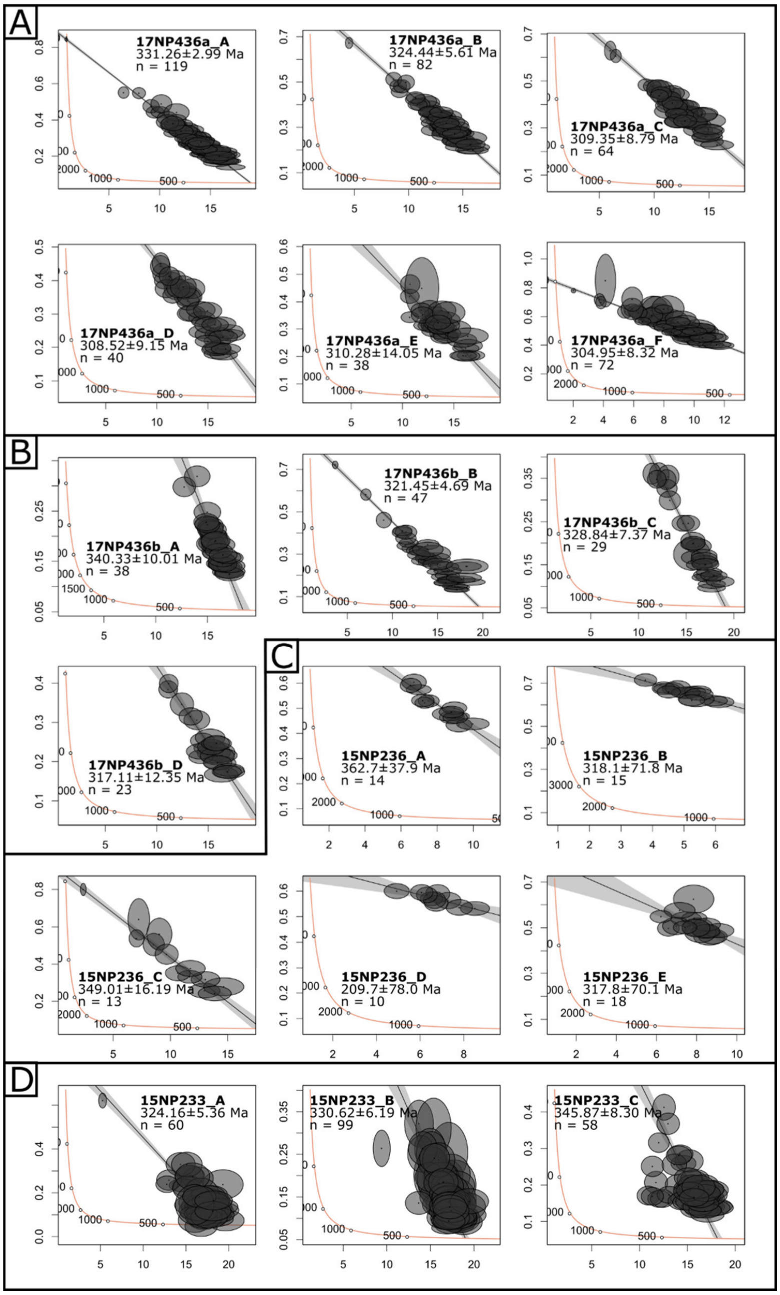

Figure C1. Tera-Wasserburg plots of age data for individual ablation areas: 17NP436a (A), 17NP436b (B), 15NP236 (C), 15NP233 (D).

https://doi.org/10.5194/gchron-2021-27
Preprint. Discussion started: 20 September 2021

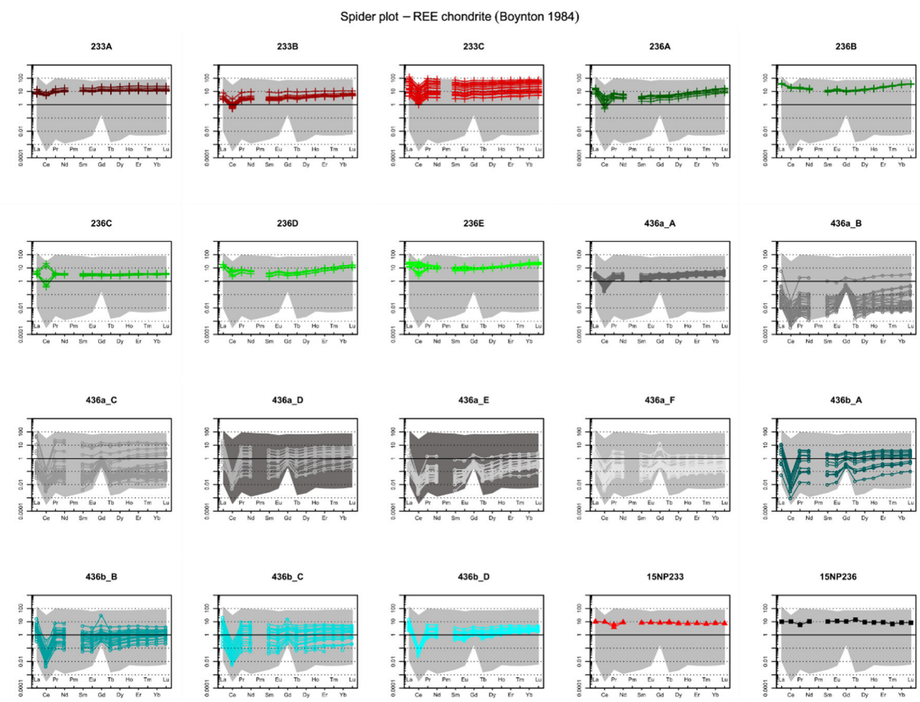

Figure D1. Rare earth element plots of each individual ablation area. 15NP233 and 15NP236 whole rock data from Rembe et al. (2021).